

# In situ ionospheric observations near lunar south pole by the Langmuir Probe on Chandrayaan-3 lander

G. Manju<sup>1</sup>, Tarun Kumar Pant,<sup>1</sup> N. Mridula,<sup>1</sup> Md. Mosarraf Hossain,<sup>1</sup> K. M. Ambili<sup>1</sup>, P. Pradeep Kumar,<sup>2</sup> T. V. Sruthi,<sup>1,3</sup> K. S. Vishnupriya,<sup>1,3</sup> R. Satheesh Thampi,<sup>1</sup> A. N. Aneesh,<sup>1</sup> Keshav Ram Tripathi<sup>1,4</sup>, P. Sreelatha<sup>5</sup> and Rosmy John<sup>2</sup>

<sup>1</sup>Space Physics Laboratory (SPL), VSSC, Trivandrum 695022, India

<sup>2</sup>Avionics, VSSC, Trivandrum 695022, India

<sup>3</sup>University of Kerala, Department of Physics, Trivandrum 695022, India

<sup>4</sup>University of Tokyo, Department of Complexity Science and Engineering, Tokyo 113-8654, Japan

<sup>5</sup>HRDD, MSA, VSSC, Trivandrum 695022, India

Accepted 2025 July 31. Received 2025 July 28; in original form 2025 February 17

## ABSTRACT

*In situ* measurements of the near surface lunar plasma environment are made using the RAMBHA-LP (Radio Anatomy of the Moon Bound Hypersensitive ionosphere and Atmosphere-Langmuir Probe) payload onboard India's Chandrayaan-3 Lander during lunar daytime (2023 August 24 to 2023 September 2). These observations provide estimates of near surface (2 m above the surface) lunar electron density and electron temperature from the south polar region, 'for the first time'. The estimations reveal the daytime lunar plasma to have mean electron density ( $N_e$ ) in the range of 380–600/cc and mean electron temperature ( $T_e$ ) in the range of 3000–8000 K. The critical roles of solar wind and the Earth's magnetospheric particle flux in modulating the lunar dayside ionosphere outside and inside the Earth's geomagnetic tail, respectively, are unravelled using RAMBHA-LP observations and lunar ionospheric model simulations. The study also highlights the role of molecular species in the genesis of lunar near surface plasma environment.

**Key words:** plasmas – solar wind – planets and satellites: atmospheres.

## 1 INTRODUCTION

The Moon, having gravity, 1/6th of the Earth, is devoid of an inherent global magnetic field and sustains a tenuous but still detectable neutral atmosphere (Hodges, Hoffman & Johnson 1974; Stern 1999; Sridharan et al. 2010a; Dhanya et al. 2021; Ambili & Choudhary 2022). This tenuous neutral atmosphere designated as surface bound exosphere (SBE) also sustains a tenuous ionosphere/plasma. The presence of a plasma environment, termed as lunar ionosphere, has been observed at altitudes as high as 3 km and beyond (Imamura et al. 2012; Choudhary et al. 2016; Halekas et al. 2018). Direct photoionization of neutral species through solar irradiation constitutes the major source. Solar wind (SW) particles, sputtered charged particles from surface, metallic ions from meteoric impacts and charged lunar dust are also recognized as important sources of the lunar ionosphere (Stubbs et al. 2011), while surface absorption and convective electric field pickup and eventual removal are two major loss processes (Bauer 1996; Ambili & Choudhary 2022).

Existence of a lunar ionosphere, with  $N_e$  of 1000/cc, was first indirectly deduced during lunar occultation events (Andrew, Branson & Wills 1964). However, observational evidences for a lunar ionosphere came during multiple Apollo missions, when Charged

Particle Lunar Environment Experiment's (CPLEE) ion-electron spectrometer and Supra-thermal Ion Detector Experiment's (SIDE) mass spectrometers were operated on the lunar surface (Freeman & Hills 1970; O'Brien & Reasoner 1971, Benson, Freeman & Hills 1975).

Concurrently, though the Radio Occultation (RO) technique confirmed the presence of lunar ionosphere, the estimates were far from consistent. These reported measurements, suggested electron densities ( $N_e$ ) as follows: (i)  $N_e \leq 40/\text{cc}$  (Pomalaza-Diaz 1967; Vyshlov 1976), (ii)  $N_e$  of around 500–1000/cc (Vasil'Ev 1974; Vyshlov & Savich 1979), (iii)  $N_e$  of around 300/cc (Imamura et al. 2008, 2010; Ando et al. 2012), (iv) peak  $N_e$  of around 300/cc on the day side (Choudhary et al. 2016), (v)  $N_e$  of  $10^4/\text{cc}$ , and (vi)  $N_e$  of around  $10^3/\text{cc}$  in the lunar wake and terminator (Tripathi et al. 2022) respectively.

In contrast to these studies on lunar electron density, few reports exist on lunar electron temperature, and they focus on the photoelectron sheath. The photoelectric yield measurements on the samples brought during the Apollo missions showed that the rate of photoelectron emission was  $4.5 \text{ A/m}^2$  and the electron mean kinetic energy was  $\approx 2 \text{ eV}$  ( $\approx 2.3 \times 10^4 \text{ K}$ ) (Feuerbacher et al. 1972; Nitter, Havnes & Melandsø 1998). The lunar prospector had an Electron Reflectometer, an electrostatic analyser, that measured the complete 3D electron distribution functions in the energy range from 7–38 eV

\* E-mail: manju\_spl@vssc.gov.in

to 20 keV, spanning all look directions (Halekas et al. 2008). This instrument thus sampled electrons at relatively larger electron energy ranges of 7 eV ( $\approx 8.1 \times 10^4$  K) and above.

Recently, Choudhary et al. (2016) carried out a modelling study using a photochemical model and the measured neutral densities on Moon (Sridharan et al. 2010a), and suggested that molecular ions might predominate the lunar ionosphere. Later, Ambili & Choudhary (2022) used a fluid-based photochemical model called lunar ionospheric model (LIM) and showed that lunar  $N_e$  maximized at night over the poles and that the plasma distribution was essentially controlled by photochemistry with the SW remaining a strong removal agent. The model is based on the premise that plasma production over the Moon is due to two important factors: (1) photo production and (2) SW protons and electron charge exchange reactions. Over the poles, even during the midnight, the solar zenith angle (SZA) is not zero, and significant production occurs. Moreover, another important contribution come from SW/magnetospheric particle charge exchange reactions. Another aspect is that, during nighttime, due to the low temperature, the maximum neutral density is near to the surface. CO<sub>2</sub> and H<sub>2</sub>O show midnight maxima. All these factors lead to maximum electron density at night over the lunar poles (Ambili & Choudhary 2022).

One interesting aspect of the variability in the lunar ionosphere occurs when the Moon traverses the geomagnetic tail. During the course of one lunar day, the Moon cruises through the geomagnetic tail for few Earth days, the exact duration (within the geomagnetic tail) depending upon the interplanetary parameters like SW and its dynamic pressure. Halekas et al. (2018) used measurements of electron plasma frequency oscillations from the two-probe experiment in the ARTEMIS (Acceleration, Reconnection, Turbulence, and Electrodynamics of Moon's Interaction with the Sun) mission, as the Moon traversed the geomagnetic tail and reported a tenuous ionosphere with  $N_e$  of 0.1–0.3/cc. Statistical analyses and case studies using *in situ* measurements during the ARTEMIS mission revealed densities lower than 35/cc in the altitude region of 10–50 km over the Moon (Shen, Halekas & Poppe 2023).

In short, a vast majority of the lunar ionospheric measurements have been carried out using radio occultation, providing estimates of  $N_e$  at altitudes  $> 3$  km from the surface, thus leaving the understanding of near surface plasma density/processes open. In such a scenario, the Radio Anatomy of Moon Bound Hypersensitive ionosphere and Atmosphere-Langmuir Probe (RAMBHA-LP) onboard Chandrayaan-3 Vikram lander was conceived and flown with objective of obtaining *in situ* measurements of the lunar near surface plasma, for the first time ever, from the near south polar landing site ( $70^\circ$  S,  $32^\circ$  E). RAMBHA-LP provided estimates on the near surface lunar electron density and its temporal evolution through direct measurements, when the Moon was outside and within the geomagnetic tail. This report presents these measurements in detail. The LIM model was used to simulate the near surface ionosphere at the landing site.

## 2 METHODS

The details on the data and methodology used for the analysis are discussed in this section.

### 2.1 Data

Chandrayaan-3, the second Indian lunar lander mission, successfully soft-landed on Moon on 2023 August 23. The results from RAMBHA-LP payload operated in the default sweep mode, from

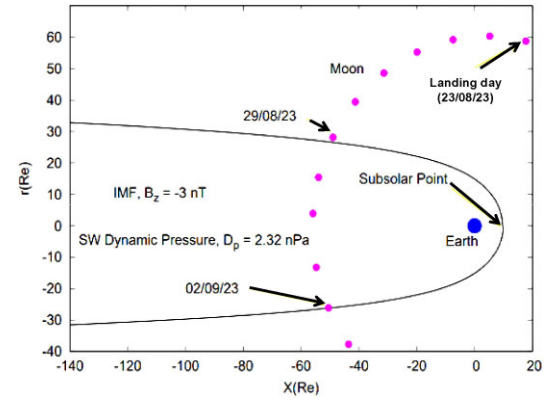


**Figure 1.** The position of the Moon with respect to the geomagnetic tail during the period from 2023 August 23 to 2023 September 3.

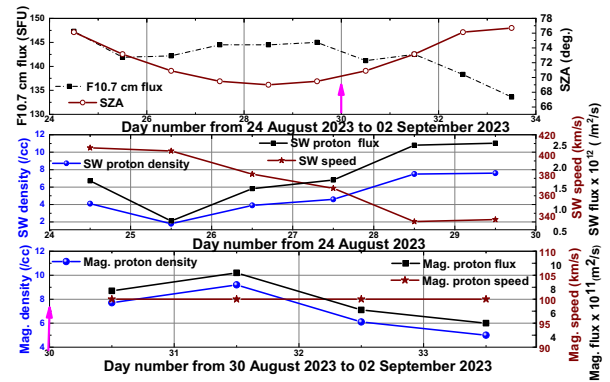


**Figure 2.** (a) The temporal variation of F10.7 cm flux and (SZA) during 2023 August 24 to 2023 September 2. (b) The temporal variation of SW proton number density, speed, and flux during 2023 August 24 to 2023 August 29. (c) The magnetospheric proton number density, speed, and flux during the period when Moon was inside the geomagnetic tail.

2023 August 24 to 2023 September 2 (a fraction of a lunar day, adding up to 10 Earth days) is reported herein. In this mode the probe operated in the  $\pm 12$ V range in steps of 0.1 V. Estimation of electron density and electron temperature were made during the mission using the data. In order to interpret the estimated plasma parameters and their temporal variations, the position of the Moon with respect to the geomagnetic tail was examined. Fig. 1 illustrates the position of the Moon with respect to the geomagnetic tail during the period from 2023 August 23 to 2023 September 3 (i.e. fraction of a lunar day) estimated using SW and interplanetary magnetic field (IMF) parameters from ACE satellite located at L1 point. The pink arrow in Figs 2–4 represents the time of the Moon's entry into the geomagnetic tail.

### 2.2 LIM model

The lunar ionosphere at Chandrayaan-3 lander, Vikram, landing site, in view of the present observations, is simulated using a 3D-LIM model. It considered an SBE consisting of 10 species namely CO<sub>2</sub>, CO, H<sub>2</sub>O, OH, O, Ar, He, Ne, CH<sub>4</sub>, and H<sub>2</sub>. Two transport processes, namely (a) SW sweeping when the Moon is outside the geomagnetic tail and (b) geomagnetic field effect when the Moon is inside the geomagnetic tail are included in the model. The SW sweeping refers to pickup of near-surface lunar ions by electromagnetic forces related

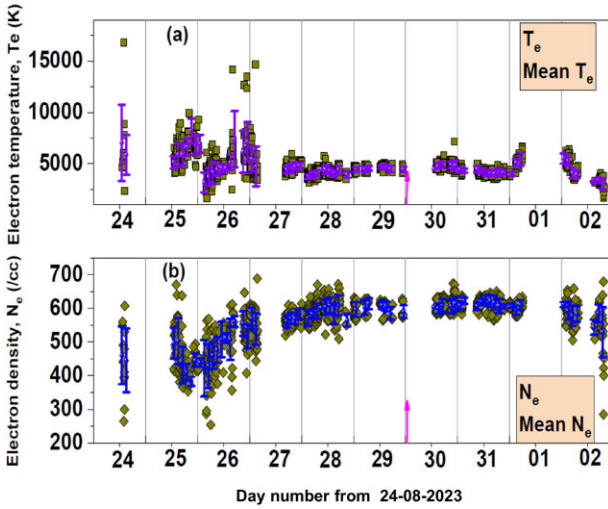


**Figure 3.** Temporal variations of (a) electron temperature ( $T_e$ ) and its 2 hourly mean and (b) electron density ( $N_e$ ) and its 2 hourly mean during the period from 2023 August 24 to 2023 September 2.

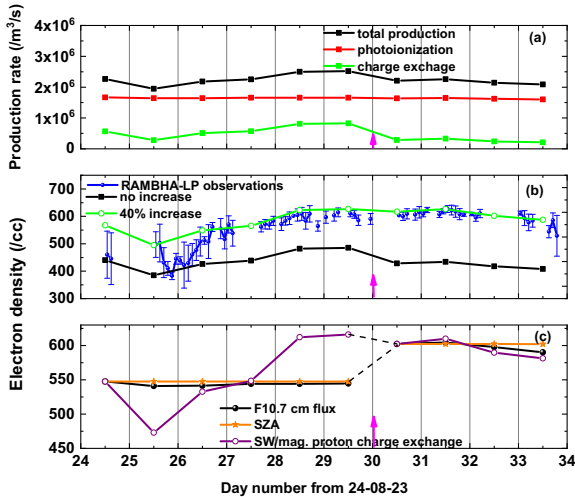


**Figure 4.** (a) Time variation of production rate due to photoionization, SW/magnetospheric charge exchange, and total production rate. (b) Time variation of mean  $N_e$  from RAMBHA-LP observations and the LIM simulated  $N_e$ . (c) Successive Model simulations by varying F10.7 cm flux, SZA, and SW/magnetospheric charge exchange while maintaining other parameters the same.

to the flow of the SW past the moon. In the magnetotail, the diffusion along geomagnetic field lines is effective. Accordingly, the lunar plasma flows along geomagnetic field lines that stretches away from Moon when it is inside the magnetosphere. This effectively acts as a loss process for the ambient plasma.

The LIM model estimates the contributions from processes such as photoionization, photoelectron impact ionization, SW charge exchange, radiative/dissociative recombination, and ion-atom interchange reactions to simulate the lunar ionosphere through 16 different ions formation scheme (Choudhary et al. 2016; Ambili & Choudhary 2022). As reported by Hodges (1973) the solar longitudinal variation in neutral density in the lunar polar region is minimum. Therefore, at the Chandrayaan-3 lander location, only Ar (condensable gas) is having a strong and clear diurnal variation with maximum at the sunrise and sunset terminators with day and

nightside minimum density (Dhanya et al. 2021; Hodges 1975; Benna et al. 2015) compared to other neutrals in the model. Non-condensable gases like H<sub>2</sub> and He have maximum density during the nightside and minimum during the dayside (Ambili & Choudhary 2022). The mass spectrometer onboard Chandrayaan-1 Moon Impact Probe detected significant amounts of CO<sub>2</sub> and H<sub>2</sub>O density in the lunar exosphere (Sridharan et al. 2010b, 2015). Since H<sub>2</sub>O and CO<sub>2</sub> are non-condensable gases the same behaviour reported for H<sub>2</sub> and He applies to these species also. The abundance of CO<sub>2</sub> in the exosphere was also later reported by Lunar Atmosphere and Dust Environment Explorer (LADEE), Lunar Reconnaissance Orbiter (LRO), and ARTEMIS missions (Cook et al. 2013; Halekas et al. 2015; Poppe, Halekas & Harada 2022). Hence, the assumption of negligible longitudinal variability in neutral densities during the observation period is considered valid. The total default neutral density used in LIM is  $2.3 \times 10^6$ /cc and the enhanced total neutral density is  $3 \times 10^6$ /cc for the entire duration of the Chandrayaan-3 mission. The inclusion of these molecular species into the model, over and above the inert gas-dominated neutral environment considered in earlier studies, has revealed the presence of significant amount of molecular ions in the lunar near-surface environment.

The solar flux and SZA are two important parameters that control ionospheric production through photoionization. Fig. 2(a) illustrates the temporal variation of F10.7 cm flux, which is a proxy for solar EUV flux and SZA during 2023 August 24 to 2023 September 2. The F10.7 cm flux decreased from 147 Solart Flux Unit (SFU) on 2023 August 24 to 142 SFU on 2023 August 25 and by 2023 August 27, attained a broad peak of 145 SFU before progressively decreasing to 133 SFU on 2023 September 2. The SZA, decreased from  $76^\circ$  on 2023 August 24 to  $69^\circ$  on 2023 August 28 before increasing to  $77^\circ$  by 2023 September 2.

Outside the geomagnetic tail, the SW charge exchange process is significant and is controlled by SW flux and the ambient neutral density. The SW flux is directly dependent on the proton density and speed. The SW protons impacting the lunar surface deposit charge on to lunar neutral atoms, creating charged molecular/atomic ions. The temporal evolution of SW charge exchange reaction in terms of the above parameters is examined using LIM. The production frequency of ions by charge exchange with SW protons is proportional to the product of neutral density and SW flux (where SW flux is the product of SW speed and proton number density; Ambili & Choudhary 2022). Fig. 2(b) shows the temporal variation of SW proton density, SW particle speed and SW flux during 2023 August 24 to 2023 August 29. SW plasma speed showed an overall decreasing trend from more than  $400$  to  $335$  km s<sup>-1</sup>. The SW proton density showed an initial decrease (from  $4$ /cc to  $2$ /cc) during 2023 August 24 to 2023 August 25 followed by a gradual increase to attain a maximum of  $7.5$ /cc by 2023 August 28, which persisted till 2023 August 29. The SW flux showed a variation similar to that of the SW proton density, indicating the latter's dominant role in controlling the former.

In the geomagnetic tail, the magnetospheric protons impacting the lunar surface, deposit charge onto lunar neutral atoms, creating charged molecular/atomic ions. During the period when the Moon was inside the geomagnetic tail, i.e. from 2023 August 30 to 2023 September 2, the magnetospheric proton (H<sup>+</sup> ions) flux and neutral densities are expected to control the charge exchange reactions as well as ionization therein. Accordingly, the ion density was calculated using the expression given by Daily et al. (1977). The production and loss rates of the ions were calculated to derive the ion density. The bulk velocity of the ions, an important parameter determining the loss rate inside the geomagnetic tail, was calculated considering ambient neutral temperature. Daily et al. (1977) had considered

only three atomic species, whereas in the LIM other neutrals were also considered, and the LIM simulations compared well with the estimates of the former for inert species like Argon.

The production frequency of ions by charge exchange with magnetospheric protons is proportional to the product of neutral density and magnetospheric proton flux, where magnetospheric proton flux is the product of magnetospheric proton speed and proton number density. Fig. 2(c) depicts the magnetospheric proton density, speed, and flux during the period when the Moon was inside the geomagnetic tail. Zhang (2006) had estimated magnetospheric proton ( $H^+$ -ions) speed of  $80\text{--}120 \text{ km s}^{-1}$  for distances up to  $50 R_E$  in a theoretical study on magnetospheric proton transport. In the present study, magnetospheric proton speed has been taken as  $100 \text{ km s}^{-1}$ , which is the mean of the above range of speeds for the entire period within geomagnetic tail. The maximum value of magnetospheric proton density is taken to be  $9/\text{cc}$  as reported by Liemohn, Kenney & Knaflisch (1967). In the model, the pattern of variation in the SW proton density during 2023 August 30 to 2023 September 2 is also incorporated into the magnetospheric proton density. Accordingly, the magnetospheric proton density showed an increase ( $7.5/\text{cc}$  to  $9.5/\text{cc}$ ) from 2023 August 30 to 2023 August 31 and thereafter a gradual decrease to attain a minimum value of around  $5/\text{cc}$  by 2023 September 2 (Fig. 2c). The magnetospheric proton flux showed a variation similar to that seen in the magnetospheric proton density, indicating its role in modulating the flux inside the geomagnetic tail (Fig. 2c).

### 2.3 Estimation of plasma parameters

In the default mode of operation, the RAMBHA-LP probe was swept in the  $\pm 12 \text{ V}$  range in steps of  $0.1 \text{ V}$ . The dwell time at each sample is  $60 \text{ ms}$  and the sampling rate is  $1 \text{ ms}$ . The mean of the  $60$  data points collected at each voltage step is obtained to remove the random noise. The final sweep configuration (in the range of  $\pm 12 \text{ V}$  at  $0.1 \text{ V}$  increment) obtained is used as the basic sweep for deriving the science parameters. In the analysis, the assumption of Maxwellian electron distribution is made. The ion current in the basic sweep was large ( $180 \text{ nA}$ ), and the zero-crossing point of the current was much above the inflection point near the apparent ion saturation region, indicating the contribution of photoemission current ( $I_{ph}$ ) to the ion current. The  $I_{ph}$  is estimated using a method suggested and successfully used by Johansson et al. (2017) (details given in Appendix) to process the *Rosetta* mission LP data. The  $I_{ph}$  is removed from the basic sweep, and the resultant sweep is used for plasma parameter estimation.

The lunar plasma is non-magnetized and tenuous. Although localized crustal magnetic fields are there, the Vikram lander location was free from crustal magnetic field as evidenced from previous literature (Hood, Bryant & van der Leeuw 2022). Therefore, it is ideally suited to be analysed using the OML theory for Langmuir probes. Further, the RAMBHA-LP probe being situated on the stationary Lander platform, an effect like ram velocity which influences the measurements for moving satellite based LP experiments are not relevant. Hence, the reports (Piel, Hirt & Steigies 2001; Barjatya et al. 2009) wherein researchers have used modified expressions for estimating electron density accounting for the changes in current collection in the case of magnetized, collisional plasmas and plasmas affected by ram velocity are not applicable in the case of the RAMBHA-LP on lander. Further, the ram velocity due to SW is manifesting as a factor controlling the removal of ions from the lunar ambience. The RAMBHA-LP probe which is stationary in the ambience will sense the instantaneous electron densities which

sustain therein after the SW related removal process. Overall, the RAMBHA-LP probe-based data from the Vikram lander is ideal to be processed using the classical OML theory. The characteristic length of relevance in Langmuir probe theory is the probe radius which in the case of RAMBHA-LP is  $2.5 \text{ cm}$ . The calculated smallest Debye length from the estimated mean  $N_e$  and  $T_e$  values during the mission is  $17 \text{ cm}$ . This Debye length (of  $17 \text{ cm}$ ) is 7 times higher than the probe radius and hence the Langmuir probe theory is valid in the present case (Resendiz Lira & Marchand 2021). Accordingly, for a probe (like RAMBHA-LP) with radius much less than the Debye length, the current is independent of the sheath size such that the orbital motion equation essentially provides its volt-ampere characteristics (Mott-Smith & Langmuir 1926).

For accelerating potentials, where  $I$  is the current collected by the probe at potential  $V$ ,  $I_0$  is the saturation current,  $V_s$  is the plasma potential,  $e$  is the electron charge,  $k$  is the Boltzmann constant, and  $T_e$  is the electron temperature. That is, the difference between the current and its saturation value  $I_0$  changes exponentially with the voltage. For small spheres, the current is therefore a linear function of the voltage. The plasma parameters are derived from the  $I$ - $V$  characteristic curve which is the plot of  $V$  (potential applied to LP) versus  $\ln(I)$ , where  $I$  is the current collected due to ambient charged species. The slope of the exponentially increasing portion of the  $I$ - $V$  curve is estimated and the electron temperature in eV ( $T_{eV}$ ) is assessed using equation 2 (Merlino 2007):

$$\frac{kT_e}{e} = \frac{1}{\text{slope}} \quad (2)$$

The details of the method of estimating slope are given in Section A3 of the Appendix. The normalized root mean square error (NRMSE) values of the fits of the ion saturation region and electron saturation region have been determined and the mean NRMSE is found to be  $<0.07$ , indicating the robustness of the fits. Details of determining  $V_s$  are given in Section A3 of the Appendix. It is readily observed that for  $V = V_s$  in equation (1),  $I = I_0$  (from Mott-Smith & Langmuir 1926),

$$I_0 = 0.25N_e e A v_t, \quad (3)$$

where  $v_t = (8kT_e/\pi m_e)^{0.5}$ . The electron density,  $N_e$  is obtained using the measured current  $I_0$  at the plasma potential (Merlino 2007; as given in equation 3). The letters  $k$ ,  $e$ ,  $m_e$ , and  $A$  in the above equations denote the Boltzmann constant, electron charge, electron mass, and surface area of probe.

## 3 OBSERVATIONAL RESULTS

The Moon was outside the geomagnetic tail from 2023 August 23 to 2023 August 29. By 2023 August 30, the Moon had entered the geomagnetic tail and remained therein till 2023 September 2. Figs 3(a) and (b) show the time variations of (a) electron temperature,  $T_e$  and its 2 hourly mean, (b) electron density,  $N_e$  and its 2 hourly mean, estimated from RAMBHA-LP measurements. The 2 hour interval is chosen such that the ionosphere is not likely to undergo changes therein and sufficient points are available for obtaining the mean.

Fig. 3(a) shows large  $T_e$  fluctuations in the range of  $1500\text{--}17\,000 \text{ K}$  up to 2023 August 26. From 2023 August 27 to 2023 August 29, it stabilizes at around  $4500 \text{ K}$ . On 2023 August 30, the  $T_e$  values hover around  $5000\text{--}6000 \text{ K}$  before showing a tendency to increase to more than  $6000 \text{ K}$  early on 2023 September 1. On 2023 September 2, the  $T_e$  values fall off from around  $6000 \text{ K}$  to around  $2000 \text{ K}$  by the end of that day. As seen in Fig. 3(b), the  $N_e$  values are also fluctuating

during the initial phase up to 2023 August 26, attaining values of around 680/cc before decreasing to low values of around 250/cc by 2023 August 26. Thereafter, the  $N_e$  increases to around 600/cc by 2023 August 27 and persists at that value up to 2023 September 2. By the end of 2023 September 2, the  $N_e$  values reduce to around 300/cc.

Between 2023 August 27 and 2023 August 30, the variabilities in  $N_e$  and  $T_e$  are within the error bars, while the correlated pattern of variability on 2023 September 2 may be due to effects of being near the bow shock which needs to be examined in future. To understand the temporal variations in  $N_e$  observed by RAMBHA-LP payload, the time evolution of electron density contributions from two dominant processes, namely photoionization and charge exchange, are examined. Fig. 4(a) shows the time variations of production rate due to photoionization and SW/magnetospheric charge exchange along with the total production rate during 2023 August 24 to 2023 September 2 (the former two parameters obtained from the product of the respective rate coefficients and neutral density (Ambili & Choudhary 2022). From Fig. 4(a), it is clear that the photoionization production rate is relatively constant, while SW/magnetospheric charge exchange production rate shows distinct temporal changes, thus demonstrating the important role of the latter in modulating the temporal changes in ambient ionization, although photoionization dominates overall production.

Fig. 4(b) shows the mean  $N_e$  values derived from RAMBHA-LP observations along with the 3D-LIM simulated  $N_e$  values (with default (corresponding to observations in 2008 solar minimum period) and 40 per cent enhanced neutral densities). The daily mean  $T_e$  obtained from RAMBHA-LP observations was used for the simulations. The number densities for CO<sub>2</sub> and H<sub>2</sub>O, the dominant neutral species contributing to the lunar ionosphere are enhanced by 40 per cent with respect to the previously reported measurements (default values) used for LIM by Ambili & Choudhary (2022) to account for increased solar activity during 2023 and consequent effects on neutral atmosphere. Table A1 shows the abundances of different species used for the model simulations.

RAMBHA-LP derived mean  $N_e$  values decreased from 480/cc on 2023 August 24 to 370/cc by 2023 August 25, and then gradually increased to 600/cc by 2023 August 28, thereafter remaining steady until 2023 September 1. By 2023 September 2, mean  $N_e$  values decreased to 520/cc. LIM simulations with a 40 per cent increase in neutral densities correspond well with observed  $N_e$  values, suggesting the model accurately accounted for the physical processes. The model-derived  $N_e$  variations with the default neutral densities are lower compared to the observations by 100–200/cc although the temporal pattern and order of magnitude match well.

A sensitivity study on the control of different background parameters on the  $N_e$  values is carried out (Fig. 4c). The relevant parameters are neutral densities (CO<sub>2</sub>), SZA, F10.7 cm flux, and SW/magnetospheric particle flux. The neutral densities used in the model are constant with time and hence do not contribute to the temporal variations of  $N_e$  for the observation site as mentioned earlier. This is in accordance with the previous reports of the marginal temporal variation of H<sub>2</sub> gas density at polar regions, leading to the adaptation of same variability for CO<sub>2</sub> and H<sub>2</sub>O which are also similar non-condensable gases (Ambili & Choudhary 2022; Hodges 1973). The model is run for three different cases for analysing the sensitivity to F10.7 flux, SZA, and SW/magnetospheric charge exchange. The F10.7 cm flux and SZA are successively varied while other parameters are kept constant. These simulations did not reproduce the observed temporal pattern of  $N_e$ , signifying that only their variability does not decisively modulate the temporal pattern of  $N_e$ . The actual

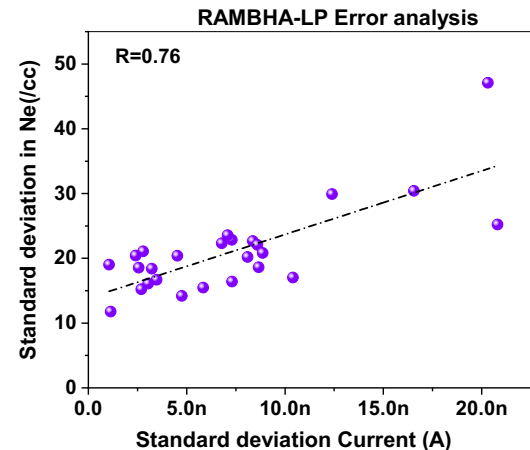


**Figure 5.** The scatter plot of the standard deviations in current and those in  $N_e$ .

variations in SW flux are estimated from L1 point measurements of SW proton number density and SW speed variations. These are considered for the simulations while the rest of the parameters are kept the same (at the value corresponding to 2023 August 24) for the period 2023 August 24 to 2023 August 29. For 2023 August 30 to 2023 September 2, magnetospheric particle flux is varied while the rest of the parameters are kept constant (at the values corresponding to 2023 August 30). The dashed lines in Fig. 4(c) demarcate the two separate simulations outside (before 2023 August 30) and inside (from 2023 August 30) the geomagnetic tail. These simulations with SW/magnetospheric charge exchange processes matched the variations of RAMBHA-LP  $N_e$  observations up to 2023 September 2. This exercise clearly demonstrates that charge exchange reaction plays the key role in modulating the temporal evolution of the lunar day side ionosphere.

#### 4 ESTIMATE OF UNCERTAINTIES FROM RAMBHA-LP OBSERVATIONS DURING CHANDRAYAAN-3 MISSION

The uncertainties in the RAMBHA-LP electron density estimates are perceived to be primarily from the current measurement uncertainties as well as random statistical errors. Here, the portion of the temporal variation of electron density (after  $I_{ph}$  removal) between 2023 August 27 and 2023 August 30 is considered wherein the  $N_e$  values are fairly steady except for the spread observed (in  $N_e$  values). During the selected period, the plasma potential values used for  $N_e$  estimation are extracted. These values are found to be fairly constant with a value of around –3 V. The spread in the current at this plasma potential of –3 V is examined in association with that in electron density. For this, the mean of the current measurements at –3 V potential is estimated for each 2-hour interval and the corresponding standard deviations are also calculated. Similarly, the mean and standard deviation of the electron density values are estimated. The scatter plot, of the standard deviations in current and  $N_e$ , is shown in Fig. 5.

It is evident that the standard deviations in current are directly related to the standard deviations in  $N_e$  with a correlation coefficient of 0.76. This relation is 99.9 per cent significant as per the *t*-test for significance. Using a two-tailed test the *p*-value is found to be < 0.01. Accordingly, for a deviation in current of around 1 nA the corresponding deviation in  $N_e$  is 15/cc. As the deviation in current increases to around 20 nA, the same for  $N_e$  turns out to be 35/cc. It

is also observed that the deviations can be as much as 50/cc for some cases. This indicates that the uncertainty of the  $N_e$  measurements could be of the order of 50/cc considering the worst-case scenario. As mentioned in Section A5 (Appendix), the maximum error in the electron density measurement in vacuum chamber for RAMBHA-LP is 40/cc as against the same (50/cc) in lunar environment. Given the fact that the actual lunar observations involved more diverse background conditions than that in the vacuum chamber the comparison in the magnitude of the random errors between them is within 20 per cent that seems reasonable. The errors in the current measurements can also contribute to the errors in electron density estimates, but these are relatively low (0.5 per cent) as mentioned earlier, for the range of currents measured using RAMBHA-LP. Hence, the random statistical errors which are larger are relevant.

## 5 SOURCES OF ERRORS IN MEASUREMENTS

The precision in Langmuir probe measurements is mainly enhanced by reducing errors in instrument design and realization rather than validity of Langmuir probe approximation with respect to observed  $I-V$  characteristics (Brace 1998). The main sources of error are (i) Contamination of probe: The RAMBHA-LP probe was kept inside the dust protection box during the transit to Moon as well as during landing process and was released from the protective box well after settlement of the lunar dust ejected due to landing, thereby ensuring that significant dust settlement was not happening on the probe. (ii) Positioning of probe with respect to spacecraft/lander-craft: Separation of the probe by 1 m from the lander craft ensured that the lander sheath effects were not affecting the measurements. From the measured densities and temperatures of RAMBHA-LP, it is found that the boom is well outside the Debye sheath thus protecting the probe from sheath effects. Regarding the probable effect of the sheath of the boom, it is to be noted that a non-conducting GFRP coupler separates the boom from the RAMBHA-LP probe and hence protects it from boom sheath effects. (iii) Non-uniform work function of the probe surface material: The fact that spherical probes are least susceptible to work function related changes in  $I-V$  characteristics (Suresh 2011) and that TiN coating (as for RAMBHA-LP probe) has very little work function variations (around 2–3 meV Lebreton et al. 2006) across the surface, ensured the probe robustness against such variations (<5 per cent). (iv) Photoelectron emission from probe: RAMBHA-LP probe data has been corrected for photoelectron emission effects by using Johansson et al. (2017) method as discussed in Section A2 of the Appendix. (v) Electronics insufficiently resolving  $I-V$  characteristics: The RAMBHA-LP sweeps were adequately sampled to generate very good sweeps during the entire mission, indicating that the specifications of the electronics system were adequate. (vi) Spacecraft not being properly grounded electrically: The Chandrayaan-3 lander had four legs and all four legs touched the lunar surface after landing and one of the legs penetrated a little deeper into the lunar regolith thus ensuring that the probe is swept in potential with respect to Lander/regolith which acts as reference. Out of all the above mentioned factors, the most relevant one for RAMBHA-LP probe is the photo emission current contribution which has been removed. Hence, it seems reasonable to conclude that the remaining error from all sources is <15 per cent.

## 6 DISCUSSION

The present results from RAMBHA-LP reveal the electron number density near the lunar surface to be 600/cc. The modelling studies using inert gas dominated lunar exosphere had earlier revealed

that long photoionization time-scales and rapid ion pick-up by the SW would limit the electron concentrations to 1/cc (Stern 1999). Other possible mechanisms for formation of an ionosphere including plasma trapping by lunar crustal magnetic fields (Savich 1976) are not applicable in a region like the Chandrayaan-3 landing site, which is devoid of any crustal magnetic field. One more aspect that needs to be discussed here is the impact of Lander exhausts during descent. RAMBHA-LP was kept inside the dust protection box during the initial phase of the launch, during the journey to Moon and the landing phase on the Moon on 2023 August 23. Later, on 2023 August 24, that is, around 24 hours after landing, RAMBHA-LP was initially switched on at zero potential followed by the deployment that resulted in the emergence of the probe from the dust protection box. Post this operation only, RAMBHA-LP started sensing the free plasma in the lunar ambience. In the context of the possibility of dust contamination post-deployment, it has been shown earlier that lunar landers consistently eject hot exhausts during the landing operations (Clegg-Watkins et al. 2016; Farrell et al. 2022). Clegg-Watkins et al. (2016) reported that the area affected by any landing mission is directly dependent on the lander mass. Following this inference, the exhaust of Vikram lander with mass 1700 kg would impact an area of 2000 m<sup>2</sup> around the landing site. Nevertheless, as per previous studies (Farrell et al. 2022) the exhaust species persist in the exosphere only for <24 hours. Since the RAMBHA-LP payload measurements commenced one day after the landing, the effect of exhaust, if any, is not expected to manifest in the measurements. In the case of contamination by sub-micron dust, one would have observed systematic reduction in the current collected by the probe during the course of the mission. The fact that RAMBHA-LP current measurements did not show any systematic degradation negates any possibility of significant dust contamination. Further, a theoretical study by Mishra & Sana (2021) showed that the dust levitation under static force equilibrium is less likely over the sunlit lunar surfaces.

The assumption of Maxwellian electron distribution has been made in the analysis and interpretation of the LP  $I-V$  characteristics. In the present case, this assumption seems valid, because for a non-Maxwellian distribution the measured RAMBHA-LP  $I-V$  curves would have either shown multiple slopes or deviation from linearity owing to the additional electron populations of different temperature and density. Further, the mean electron temperatures derived from our analysis are consistently around 5000 K, strongly indicating the dominance of thermalized Maxwellian electron population in the lunar plasma. However, in lunar ambience, additional non-thermal populations could be ascribed to (a) photoelectrons produced in the daytime lunar near surface environment and (b) photoelectrons ejected from sunlit spacecraft surfaces. Nevertheless, in order to lead to significant errors in the measurements of  $N_e$  and  $T_e$ , these non-Maxwellian electrons need to be present in significant quantities relative to the Maxwellian electrons. While the presence of non-Maxwellian electrons cannot be unambiguously ruled out, it can be said that their contribution is minimal in the present case. Further, quantitative understanding of their sources on Moon is also rather limited, especially over polar latitudes.

The RAMBHA-LP observations obtained during a part of the lunar day within and outside the geomagnetic tail are in contrast to the values of few tens/cc and <0.1/cc, respectively, reported using ARTEMIS observations (Halekas et al. 2018; Shen et al. 2023). It is to be noted that the measurements using plasma oscillations, by ARTEMIS correspond to altitudes above 10 km, while the RAMBHA-LP measurements correspond to an altitude of around 2 m. The 300/cc value reported by Chandrayaan1 RO observations (Choudhary et al. 2016) corresponded to lower solar

activity conditions at a different location (compared to Vikram landing site) and SZA. Ambili & Choudhary (2022) reported that in the presence of SW sweeping, the electron density exponentially decreases and the height of the ionosphere is restricted to 40 km. The exponential decrease of the electron density depends on the neutral density distribution that depends on the ambient neutral temperature. Here, the point is that, in the presence of SW sweeping, the electron density is of the order of hundreds of electrons per cc.

For completeness, one should also consider the possible contribution to the electron density from the photoelectron sheath. Mishra & Bhardwaj (2019) modelled the lunar photoelectron sheath structure as well as the dust levitation on the sunlit regolith and reported electron density of around 20–30/cc. Sana & Mishra (2023) also reported low values of tens of electrons/cc for the photoelectron sheath. The electron population they deal with is at a much higher temperature than the much cooler electron population (<1 eV) revealed by RAMBHA-LP.

Overall, the LIM simulations including molecular species is found to match well with the RAMBHA-LP observations. The simulations also reveal that SW/magnetospheric charge exchange processes control the temporal evolution of the lunar ionosphere during the daytime periods.

## 7 CONCLUSIONS

(1) The RAMBHA-LP measurements, carried out near polar region consistently over 10 Earth days, demonstrate that the lunar near-surface ionosphere has electron densities in the range of 600/cc. (2) LIM simulations highlight the role of molecular ions in the genesis of the lunar ionosphere. (3) The LIM simulations in association with the RAMBHA-LP observations demonstrate the decisive roles of SW charge exchange outside the geomagnetic tail and magnetospheric particle charge exchange inside the geomagnetic tail in modulating the temporal evolution of day side lunar ionosphere.

## ACKNOWLEDGEMENTS

All the authors thank ISRO for funding the project. The authors would like to put on record the immense support provided by Director, SPL, Dr. K. Rajeev during the course of the project. The prolific discussions with Prof. R. Sridharan, former Director, SPL throughout the project duration were invaluable. The authors express their gratitude to the former Directors of SPL, Dr. K. Krishnamoorthy, Prof. Anil Bhardwaj, and Dr. Radhika Ramachandran for their support and guidance during different stages of the payload development. The authors are thankful to Dr. Madhav Haridas for help in debugging the processing software for RAMBHA-LP science and Dr. R. P. Aswathy for assistance in payload testing and characterization. Assistance rendered by Dr. Dhanya M. B. during the initial design stages of RAMBHA-LP ground segment data pipeline development is gratefully acknowledged. Contributions from Mr. Santhosh Nalluveettil, Mr. Johns Paul, Mr. Sabir Alam, Mr. Nirbhay Kumar Upadhayay, Mr. Manu Thomas, and Mr. Snehil Srivasatava during RAMBHA-LP payload development, as well as Ms. Rejitha R. in ground segment data pipeline development, are acknowledged with gratitude. We would also like to express our gratitude to all scientists and engineers at different entities of VSSC/IISU who have contributed to the development of the RAMBHA-LP payload.

## DATA AVAILABILITY

The F10.7 cm flux values during the mission were obtained from omniweb.gsfc.nasa.gov. The SZA was obtained from Chandrayaan-3 mission. The SW proton number density and SW particle speed were obtained from ACE data at L1 point (omniweb.gsfc.nasa.gov). The RAMBHA-LP data are available at ISRO's designated data repository, ISSDC.

## REFERENCES

- Ambili K. M., Choudhary R. K., 2022, *MNRAS*, 510, 3291
- Ando H. et al., 2012, *J. Geophys. Res.: Space Phys.*, 117, A8
- Andrew B. H., Branson N. J. B. A., Wills D., 1964, *Nature*, 203, 171
- Barjatya A., Swenson C. M., Thompson D. C., Wright K. H., Jr, 2009, *Rev. Sci. Instr.*, 80, 041301
- Bauer S. J., 1996, *Anzeiger Abt. II*, 133, 17
- Benna M., Mahaffy P. R., Halekas J. S., Elphic R. C., Delory G. T., 2015, *Geophys. Res. Lett.*, 42, 3723
- Benson J., Freeman J. W., Hills H. K., 1975, *Proc. Lunar Sci. Conf.*, 6, 3013
- Brace L. H., 1998, *Meas. Tech. Space Plasmas: Particles*, 102, 23
- Choudhary R. K. et al., 2016, *Geophys. Res. Lett.*, 43, 10
- Clegg-Watkins R. N., Jolliff B. L., Boyd A., Robinson M. S., Wagner R., Stopar J. D., Plescia J. B., Speyerer E. J., 2016, *Icarus*, 273, 84
- Cook J. C., Stern S. A., Feldman P. D., Gladstone G. R.I., Rutherford K. D., Tsang C. C. C., 2013, *Icarus*, 225, 681
- Daily W. D., Barker W. A., Clark M., Dyal P., Parkin C. W., 1977, *J. Geophys. Res.*, 82, 5441
- Dhanya M. B. et al., 2021, *Geophys. Res. Lett.*, 48, e2021GL094970
- Farrell W. M., Prem P., Tucker O. J., Hurley D. M., Cohen B. A., Benna M., 2022, *Icarus*, 376, 114857
- Feuerbacher B. et al., 1972, *Proc. Lunar Sci. Conf.*, 3, 2655
- Freeman J. W., Hills H. K., 1970, *Am. Geophys. Un.*, 51, 821
- Halekas J. S., Delory G. T., Lin R. P., Stubbs T. J., Farrell W. M., 2008, *J. Geophys. Res.: Space Phys.*, 113, A9
- Halekas J. S., Delory G. T., Farrell W. M., Angelopoulos V., McFadden J. P., Bonnell J. W., Fillingim M. O., Plaschke F., 2011, *J. Geophys. Res.*, 116, A07103
- Halekas J. S., Benna M., Mahaffy P. R., Elphic R. C., Poppe A. R., Delory G. T., 2015, *Geophys. Res. Lett.*, 42, 5162
- Halekas J. S., Poppe A. R., Harada Y., Bonnell J. W., Ergun R. E., 2018, *Geophys. Res. Lett.*, 45, 9450
- Harang S. S., 2017, Master's thesis, University of Oslo
- Hodges R. R., Jr, 1973, *J. Geophys. Res.*, 78, 8055
- Hodges R. R., Jr, 1975, *Moon*, 14, 139
- Hodges R. R., Jr, Hoffman J. H., Johnson F. S., 1974, *Icarus*, 21, 415
- Hood L. L., Bryant I., van der Leeuw J., 2022, *Geophys. Res. Lett.*, 49, e2022GL100557
- Imamura T. et al., 2008, *Earth Planets Space*, 60, 387
- Imamura T. et al., 2010, *Space Sci. Rev.*, 154, 305
- Imamura T. et al., 2012, *J. Geophys. Res.: Space Phys.*, 117, A6
- Johansson F. L. et al., 2017, *MNRAS*, 469, S626
- F.Lebreton J. P. et al., 2006, *Planet.Space Sci.*, 54, 472
- Liemohn H. B., Kenney J. F., Knaflisch H. B., 1967, *Earth Planet. Sci. Lett.*, 2, 360
- Manju G. et al., 2020a, *Curr. Sci.*, 118, 383
- Manju G. et al., 2020b, *J. Atmos. Sol.-Terr. Phys.*, 199, 105203
- Manju G. et al., 2023, *J. Geophys. Res. Space Phys.*, 128, e2022JA030903
- Merlino R. L., 2007, *Am. J. Phys.*, 75, 1078
- Mishra S. K., Bhardwaj A., 2019, *ApJ*, 884, 5
- Mishra S. K., Sana T., 2021, *MNRAS*, 508, 4332
- Mott-Smith H. M., Langmuir I., 1926, *Phys. Rev.*, 28, 727
- Nitter T., Havnes O., Melandsø F., 1998, *J. Geophys. Res. Space Phys.*, 103, 6605
- O'Brien B. J., Reasoner D. L., 1971, *Apollo*, 14, 193
- Piel A., Hirt M., Steigies C. T., 2001, *J. Phys. D: Appl. Phys.*, 34, 2643

- Pomalaza-Diaz J. C., 1967, Scientific Report SU-SEL-67-095. Stanford Univ., Stanford, CA
- Poppe A. R., Piquette M., Likhanskii A., Horányi M., 2012, *Icarus*, 221, 135
- Poppe A. R., Halekas J. S., Harada Y. A., 2022, *J. Geophys. Res. Planets*, 127, e2022JE007422
- Resendiz Lira P. A., Marchand R., 2021, *Earth Space Sci.*, 8, e2020EA001344
- Sana T., Mishra S. K., 2023, *Planet. Sci. J.*, 4, 158
- Savich N. A., 1976, *Space Res.*, 16, 941
- Shen H. W., Halekas J. S., Poppe A. R., 2023, *ApJ*, 958, 165
- Sridharan R., Ahmed S. M., Pratim Das T., Sreelatha P., Pradeepkumar P., Naik N., Supriya G., 2010a, *Planet. Space Sci.*, 58, 1567
- Sridharan R., Ahmed S. M., Pratim D. T., Sreelatha P., Pradeepkumar P., Naik Neha, Supriya G., 2010b, *Planet. Space Sci.*, 58, 947
- Sridharan R., Ahmed S. M., Das T. P., Sreelatha P., Pradeep Kumar P., Naik N., Supriya G., 2015, *Planet. Space Sci.*, 111, 167
- Stern S. A., 1999, *Rev. Geophys.*, 37, 453
- Stubbs T. J., Vondrak R. R., Farrell W. M., 2005, in Krueger H., Graps A., eds, Workshop on Dust in Planetary Systems (ESA SP-643). Kauai, Hawaii, p. 181
- Stubbs T. J., Glenar D. A., Farrell W. M., Vondrak R. R., Collier M. R., Halekas J. S., Delory G. T., 2011, *Planet. Space Sci.*, 59, 1659
- Suresh P., 2011, All Graduate Theses Dissertations. Utah State University, Logan, Utah, p. 902
- Tripathi K. R., Choudhary R. K., Ambili K. M., Manikantan R., Parikh U., 2022, *MNRAS*, 515, L61
- Vasil'Ev M. B., 1974, *Cosmic Res.*, 12, 102
- Vyshlov A. S., 1976, *Space Res.*, 16, 945
- Vyshlov A. S., Savich N. A., 1979, *Cosmic Res.*, 16, 551
- Zhang M., 2006, *J. Geophys. Res.: Space Phys.*, 111, A4

## APPENDIX A

### A1 RAMBHA-LP system details

The RAMBHA-LP payload components are the mechanical system, electronics system, and lander craft. The RAMBHA-LP mechanical system was constituted with a CFRP boom hinged on a hinge L Bracket mounted below the top deck of Lander. The LP was a stemmed hollow sphere of 50 mm diameter, made of Ti alloy material with TiN coating and was kept inside the dust protection box till deployment (after landing on the lunar surface) after which the 1-m-long boom ensured the immersion of the probe in the free lunar plasma. The RAMBHA-LP electronics system comprised of an Onboard Controller (ROC), catering to the major tasks of providing probe bias potential, signal acquisition (from the probe), followed by its digitization, packetization, and transmission/reception to/from the spacecraft, including telecommand, telemetry (TM), and baseband data handling (BDH) controls. The default mode of operation after deployment entailed initial operation of the probe in zero potential mode for around 35 min followed by automatic changeover to sweep mode operation in the  $\pm 12$  V mode. The details regarding the RAMBHA-LP system are reported in Manju et al. (2020a).

### A2 Photoelectron current removal

The current to the Langmuir Probe may be demarcated into three components. These are (1) ion current ( $I_i$ ), (2) electron current ( $I_e$ ), and (3) photoemission current ( $I_{ph}$ ). The photoemission current to the probe is estimated using the method given by Johansson et al. (2017), which was based on multiple LP sweeps. Harang (2017) while discussing the multiple sweep method of  $I_{ph}$  estimation from Rosetta LP showed that for sweeps with a given ion velocity and varying plasma densities, the estimation of  $I_{ph}$  is realistic. In this context, for the Chandrayaan-3 lander, which is stationary, only the

thermal velocity of ambient plasma is mainly effective in the absence of any significant electric field effects and hence the estimation of  $I_{ph}$  using multiple sweeps as given in Johansson et al. (2017) can be used.

For this, a portion of the ion saturation region (called selected region, S) of the  $I$ - $V$  curve that has adequate negative probe potential ( $-12$  to  $-11.5$  V) is considered wherein the electron current to the probe is expected to be insignificant. In such a situation, the total current is the sum of  $I_{ph}$  and  $I_i$ . A linear fit is applied to the S region to obtain the slope of that portion of ion saturation region. The S region has an inherent non-zero slope while the photoemission current remains constant (within a sweep) with potential, such that  $dI/dV$  is zero (Johansson et al. 2017). Hence, a scatter plot of mean ion current in the S region and the slope of the  $I$ - $V$  curve in the same region are generated for a number of sweeps. A linear fit is given to the distribution of points so obtained and this fit is extrapolated to the X-axis to obtain the ion current for zero slope. Evidently, for a slope value of zero, the current contribution in the ion region is practically due to photoemission current (Johansson et al. 2017). The photoemission current  $I_{ph}$  is thus estimated using the sweeps of different data dumps obtained on each day from 2023 August 24 to 2023 September 2. If the dump size exceeds 4 hours, the dump is split into smaller dumps. The  $I_{ph}$  values for all the dumps on each day are derived as explained above and the mean and standard deviation of the same are estimated. Those points that are outside the  $3\sigma$  range are omitted and the mean of the other points is fixed as the  $I_{ph}$  value for that day. The  $I_{ph}$  value is removed from the sweep current and it is observed that after  $I_{ph}$  removal, the zero-crossing point of the current manifests at or close to the inflection point in the ion saturation current part of the  $I$ - $V$  curve. In some cases, it tended to manifest farther away in the ion saturation region or the retardation region. In such cases it is corrected so that it is shifted close to the inflection point provided the required shift is within the  $3\sigma$  of  $I_{ph}$ . The floating potential (where ion current and electron current are equal) is identified from the  $I$ - $V$  curve obtained after removal of  $I_{ph}$ . The  $I_{ph}$  removed  $I$ - $V$  curve is analysed to derive the electron current. For this, a linear fit is applied to the ion saturation region (the region with bias voltages less than floating potential) and this fitted current is subtracted from  $I_{ph}$  removed sweep to obtain the electron current.

### A3 Estimation of plasma parameters

Fig. A1 depicts the sample  $I$ - $V$  curve obtained using RAMBHA-LP probe during Chandrayaan 3 mission. It may be noted that the raw  $I$ - $V$  curve in Fig. A1 shows large ion current as mentioned earlier. The  $I_{ph}$  estimated for observation is shown as  $-170$  nA in figure. After removal of  $I_{ph}$ , the zero current is identified and that point which is  $V_f$  is marked in Fig. A1. The ‘space potential’ ( $V_s$ ) or plasma potential is the potential at which the effective potential on the probe is zero. When the bias voltage  $V$ , on the probe is adequately negative with respect to the plasma potential  $V_s$ , the probe operates in the ion saturation current ( $I_{is}$ ) region (Merlino 2007). The retarding potential region (between the floating potential and the plasma potential) which is beyond the floating potential is identified and a linear fit is given to the exponentially increasing portion of the  $V$  versus  $\ln(I)$  curve (Merlino, 2007). When the probe bias potential is very much greater than the plasma potential it operates in the electron saturation region (Merlino 2007). The plasma potential is estimated from the linear fits applied to the linear portions of the retarding potential region and the electron saturation region (of the  $V$  versus  $\ln(I)$  curve). That is, the voltage corresponding to the intersection point of these two linear fits is the plasma potential. The mean NRMSE values of the linear fits during the entire observation period is  $<0.06$  indicating

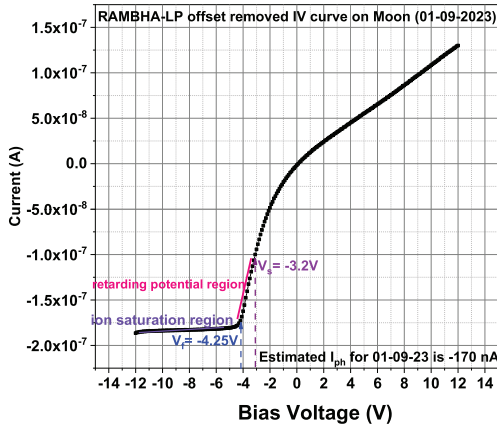


**Figure A1.** Sample  $I$ – $V$  curve obtained using RAMBHA-LP probe during Chandrayaan-3 mission.

the goodness of the fits. The slope of the exponentially increasing portion of each  $I$ – $V$  curve is estimated and the electron temperature in eV ( $T_{eV}$ ) is assessed from this slope using the equation (1). It may be noted that for slope estimation, the points within 1 V (around 10 points) from the floating potential are considered taking care to avoid the region where the deviation from linearity occurs. Further, each curve is visually examined while each data dump is processed to ensure that spurious or distorted curves (<1 per cent of total sweeps) are not wrongly fitted. It is also realized that the method of estimating plasma potential used here is more stable against random fluctuations in the sweeps rather than the other method of finding the maximum in the  $dI/dV$  values of the sweep which is susceptible to noise related fluctuations (in the sweep). Thereafter, the electron density,  $N_e$  is obtained using the measured current  $I$  at the plasma potential (as given in equation (3) mentioned earlier in main paper). The different regions like ion saturation region and retarding potential region as well as floating potential and plasma potential used for estimating plasma parameters are marked in Fig. A1. The floating potential and plasma potential for the sample curve are  $-4.15\text{V}$  and  $-3.0\text{V}$ . The past studies on lunar surface charging reveal that for latitudes close to Vikram lander landing site for the SZAs of  $66^{\circ}$ – $77^{\circ}$  (values applicable for Chandrayaan-3 mission period) potentials of the order of 20V, prevail during daytime depending on SW conditions (Stubbs et al., 2005; Halekas et al., 2011; Poppe et al., 2012). These values are comparable to the values reported herein.

#### A4 Sensitivity of probe to currents in the designed dynamic range

With regard to the capability of the instrument to sense electron densities over the entire design range of up to 10 000 /cc extensive tests were undertaken with calibrated current source in the laboratory. The RAMBHA-LP dynamic range corresponding to an electron density range of up to 10 000 /cc was 25 pA to 25  $\mu\text{A}$ . Accordingly, if the probe is able to measure currents in this range it would logically be detecting the above range of electron densities also. For the laboratory test using the current source, we have directly fed the currents to the spherical probe and the currents so sensed by the probe were measured using the electronics. The actual observed errors in the measured currents with respect to the input current were evaluated during the Test and Evaluation (T&E) of the payload. In this manuscript, the  $50\text{ K}\Omega$  resistor is used for processing the data and as per the Test & Evaluation report, the measured error in the sensed

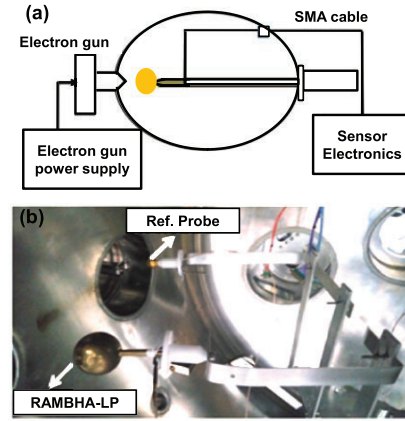


**Figure A2.** (a) RAMBHA-LP test set-up. (b) Photograph of RAMBHA-LP and reference probe during vacuum chamber test.

currents for that resistor is around 0.5 per cent. The other factor that can contribute to error in measurements from the two probes is the ambient pressure in the test chamber during the two experiments. It was ensured that identical background pressure of  $10^{-6}$  Torr was maintained during the two sets of experiments. All other parameters pertaining to the electron source were also maintained constant for the two experiments. As a consequence, the errors in measurements due to differing background pressures are not expected during the experiments. In such a scenario, the errors that can come into play are those due to error in current measurement by electronics and random statistical errors.

#### A5 Validation experiment to test sensitivity to plasma medium in vacuum chamber

The objective of the validation experiment was to demonstrate that the RAMBHA-LP and the reference probe give comparable values of the measured parameters ( $T_e$  and  $N_e$ ) for the plasma generated during the course of the experiment. The reference LP probe had been flown onboard sounding rockets from Thumba, a dip equatorial station in India earlier (Manju et al. 2020b, 2023). The control probe was a spherical brass probe (coated with gold) of 20 mm diameter with a non-conducting Teflon holder mounted on a metallic rod. It is realized that the lunar conditions of low energy, unmagnetized plasma cannot be simulated in our laboratory and the present tests are undertaken to confirm that RAMBHA-LP and the reference probe give comparable results under identical conditions. The test set-up used is shown in Fig. A2(a). The High Vacuum Space Simulation Facility consists of a 1-m long vacuum chamber provided with an electron source. The electron source from Kimball Physics, operated at 70 eV, with source voltage = 500 V and first anode voltage = 100 V.

The RAMBHA-LP is tested in the vacuum chamber along with the reference probe, with both the probes being kept inside chamber using a fixture as shown in Fig. A2(b). The probes are positioned in the vacuum chamber and the electronics is positioned outside. The effect of magnetic field on the chamber contents is avoided by orientating the electron source appropriately. The probes are successively exposed to the impinging electrons from the source. The current sensed from the probe through the SMA cable is measured by the electronics. The emission current of the electron source is varied in the range of 0.05–0.55  $\mu\text{A}$  such that the current sensed by the electronics through the probe varies. The current collected by both the probes are measured as the probes are given sweep potentials in

**Table A1.** Neutral density values used for model simulations.

Species	Density (/cc)	Enhanced density (/cc)
CO2	1.07202E6	1.50083E6
CO	107674.7	10764.7
H2O	819331.13	1.14706E6
O	42533.07	42533.07
OH	196200.7	196200.7
H2	72.34	72.34
Ar	29100.79	29100.79
He	3371.81	3371.81
Ne	5843.28	5843.27637
CH4	343.89	343.89301
Total	2.27649E6	3.03303E6

the range of  $\pm 12$  V. The electron temperature and electron density are estimated from the  $I$ - $V$  curve for each emission current value for

the up-sweep and down-sweep portions of each sweep (for gain 1 and gain 64 channels). The mean values of the electron temperature and electron density estimates for each emission current value for both gain channels and sweeps are estimated with the standard deviations. The percentage deviation of  $N_e$  and  $T_e$  for RAMBHA-LP with respect to the reference probe is within 15%, considering all the measurement samples. The maximum error (standard deviation) in the electron density measurement in vacuum chamber for RAMBHA-LP is found to be 40/cc. Overall, the experiment clearly demonstrates that the RAMBHA-LP instrument is capable of giving measurements comparable (within the error bars) to the measurements made by the reference probe.

This paper has been typeset from a TeX/LaTeX file prepared by the author.